1-1-2010

Directional control of infrared antenna-coupled tunnel diodes

Brian A. Slovick
University of Central Florida

Jeffrey A. Bean
University of Central Florida

Peter M. Krenz
University of Central Florida

Glenn D. Boreman
University of Central Florida

Recommended Citation

Slovick, Brian A.; Bean, Jeffrey A.; Krenz, Peter M.; and Boreman, Glenn D., "Directional control of infrared antenna-coupled tunnel diodes" (2010). *Faculty Bibliography 2010s*. 805.
https://stars.library.ucf.edu/facultybib2010/805

Directional control of infrared antenna-coupled tunnel diodes

Brian A. Slovick*, Jeffrey A. Bean, Peter M. Krenz, and Glenn D. Boreman

University of Central Florida, CREOL – The College of Optics and Photonics, 4000 Central Florida Blvd., Orlando, Florida 32816, USA
*bslovick@creol.ucf.edu

Abstract: Directional control of received infrared radiation is demonstrated with a phased-array antenna connected by a coplanar strip transmission line to a metal-oxide-metal (MOM) tunnel diode. We implement a MOM diode to ensure that the measured response originates from the interference of infrared antenna currents at specific locations in the array. The reception angle of the antenna is altered by shifting the diode position along the transmission line connecting the antenna elements. By fabricating the devices on a quarter wave dielectric layer above a ground plane, narrow beam widths of 35° FWHM in power and reception angles of ± 50° are achieved with minimal side lobe contributions. Measured radiation patterns at 10.6 μm are substantiated by electromagnetic simulations as well as an analytic interference model.

OCIS codes: (040.3060) Infrared; (110.5100) Phased-array imaging systems.

References and links

1. I. Codreanu, C. Fumeaux, D. Spencer, and G. Boreman, "Microstrip antenna-coupled infrared detector," Electron. Lett. **35**(25), 2166–2167 (1999).
2. C. Fumeaux, J. Alda, and G. D. Boreman, "Lithographic antennas at visible frequencies," Opt. Lett. **24**(22), 1629–1631 (1999).
3. C. Middlebrook, P. Krenz, B. Lail, G. Boreman,, "Infrared Phased-Array Antenna," Microw. Opt. Technol. Lett. **50**(3), 719–723 (2008).
4. T. Kosako, Y. Kadoya, and H. F. Hofmann, "Directional control of light by a nano-optical Yagi-Uda antenna," Nat. Photonics **4**(5), 312–315 (2010).
5. A. G. Curto, G. Volpe, T. H. Taminiau, M. P. Kreuzer, R. Quidant, and N. F. van Hulst, "Unidirectional emission of a quantum dot coupled to a nanoantenna," Science **329**(5994), 930–933 (2010).
6. C. Middlebrook, M. Roggemann, G. Boreman, N. Subotic, K. Cooper, W. Buller, W. Yang, and J. Alda, "Measurement of the Mutual Coherence Function of an Incoherent Infrared Field with a Gold Nano-wire Dipole Antenna Array," Int. J. Infrared Millim. Waves **29**(2), 179–187 (2008).
7. J. R. Fienup, "Lensless coherent imaging by phase retrieval with an illumination pattern constraint," Opt. Express **14**(2), 498–508 (2006).
8. A. W. Lee, and Q. Hu, "Real-time, continuous-wave terahertz imaging by use of a microbolometer focal-plane array," Opt. Lett. **30**(19), 2563–2565 (2005).
9. E. L. Dereniak, and D. G. Crowe, *Optical Radiation Detectors*, (John Wiley & Sons, New York, 1984).
10. P. M. Krenz, B. A. Lail, and G. D. Boreman, "Calibration of Lead-Line Response Contribution in Measured Radiation Patterns of IR Dipole Arrays," IEEE J. Quantum Electron. (to be published).
11. S. Y. Yang, T. Izawa, and T. K. Gustafson, "Coupling characteristics of thin-film metal-oxide-metal diodes at 10.6 μm," Appl. Phys. Lett. **27**(9), 481 (1975).
12. M. Abdel-Rahman, F. González, and G. Boreman, "Antenna-coupled metal-oxide-metal diodes for dual-band detection at 92.5 GHz and 28 THz," Electron. Lett. **40**(2), 116 (2004).
13. J. A. Bean, B. Tiwari, G. H. Bernstein, P. Fay, and W. Porod, "Long wave infrared detection using dipole antenna-coupled metal–oxide–metal diodes," J. Vac. Sci. Technol. B **27**(1), 11 (2009).
14. C. A. Balanis, *Antenna Theory: Analysis and Design*, (John Wiley & Sons, New York, 1997).
15. J. Bean, B. Slovick, and G. Boreman, "Influence of substrate configuration on the angular response pattern of infrared antennas," Opt. Express. submitted.
16. D. B. Rutledge, and M. S. Muha, "Imaging antenna arrays," IEEE Trans. Antenn. Propag. **30**(4), 535–540 (1982).
17. I. Codreanu, and G. D. Boreman, "Influence of dielectric substrate on the responsivity of microstrip dipole-antenna-coupled infrared microbolometers," Appl. Opt. **41**(10), 1835–1840 (2002).
18. B. Tiwari, J. A. Bean, G. Szakmány, G. H. Bernstein, P. Fay, and W. Porod, "Controlled etching and regrowth of tunnel oxide for antenna-coupled metal-oxide-metal diodes," J. Vac. Sci. Technol. B **27**(5), 2153–2160 (2009).

19. J. Bean, A. Weeks, and G. Boreman, "Performance optimization of antenna-coupled Al/AlO$_X$/Pt tunnel diode infrared detectors," IEEE J. Quantum Electron. submitted.
20. I. Codreanu, F. González, and G. Boreman, "Detection Mechanisms in microstrip dipole antenna-coupled infrared detectors," Infrared Phys. Technol. **44**(3), 155–163 (2003).
21. S. M. Faris, B. Fan, and T. K. Gustafson, "Electronic tunneling currents at optical frequencies," Appl. Phys. Lett. **27**(11), 629–631 (1975).
22. J. Ginn, B. Lail, D. Shelton, J. Tharp, W. Folks, and G. Boreman, "Characterizing Infrared Frequency Selective Surfaces on Dispersive Media," ACES J. **22**(1), 184–188 (2007).
23. J. Bean, B. Tiwari, G. Szakmany, G. Bernstein, P. Fay, and W. Porod, "Antenna length and polarization response of antenna-coupled MOM diode infrared detectors," Infrared Phys. Technol. **53**(3), 182–185 (2010).
24. R. L. Olmon, P. M. Krenz, A. C. Jones, G. D. Boreman, and M. B. Raschke, "Near-field imaging of optical antenna modes in the mid-infrared," Opt. Express **16**(25), 20295–20305 (2008).
25. P. Krenz, B. Slovick, J. Bean, and G. Boreman, "Alignment procedures for radiation pattern measurements of antenna-coupled infrared detectors," Opt. Eng. **49**(4), 033607-1 (2010).

1. Introduction

Infrared (IR) antenna-coupled sensors provide several advantages over conventional photonic, bolometric, and pyroelectric IR detectors. By separating the sensor from the radiation receiver, the sensor can be designed on sub-wavelength scales to reduce the response time of the detector [1]. Meanwhile, the antenna can be tailored to achieve the desired polarization and wavelength sensitivity [2]. Integration of the antenna-coupled sensor into an array allows the amplitude and phase of the collected radiation to be manipulated to achieve directional control of infrared radiation [3]. Although unidirectional control of visible radiation has been demonstrated with metal nanorod arrays and antenna-coupled quantum dots [4,5], these devices operate only in transmission or scattering mode and are limited to a narrow range of emission angles. In the thermal or long wave infrared band, the potential applications of a steerable receiving antenna-coupled sensor include coherence detection [6] and lensless imaging [7].

The angular response characteristics of antenna-coupled microbolometers are documented in the literature [3]. A common antenna design utilizes a dipole antenna pair to capture and transfer the incident radiation to the microbolometer along a coplanar strip (CPS) transmission line [3,6]. The position of the microbolometer relative to the dipoles determines the phase shift between the infrared currents. Although microbolometers are readily integrated into antenna arrays [8], the intrinsic thermal detection mechanism diminishes their ability to operate as a point load. Bolometric detection relies on a change in electrical resistance when infrared radiation is absorbed by the bolometer and converted to heat [9]. Under an applied constant current, one measures a change in voltage corresponding to a variation in optical power. With this approach, the sensitivity of the detector is determined by its temperature coefficient of resistance (TCR). If the TCR of the bolometer is not several orders of magnitude greater than the CPS, antenna, and lead-lines, the measured response will receive contributions from all, and a careful calibration procedure is required to extract the antenna response from the measured radiation pattern [10].

To address these issues, we replace the microbolometer with a metal-oxide-metal tunnel diode [11,12]. MOM diodes exhibit high IR impedance and a non-linear current-voltage (*I-V*) characteristic, and thus are capable of rectifying high-frequency antenna currents at a localized point in the array. Operation of such devices has been extended to the long wave infrared band with promising results [13]. In addition to its capability to operate as a point load, MOM diodes offer several advantages beyond conventional IR detectors, including functionality without a bias voltage, operation at room temperature without cooling, and CMOS compatible fabrication.

Similar to the analysis of radio frequency antennas, the angular response pattern of an infrared antenna is proportional to the product of an array factor and the radiation pattern of a single element [14]. By this methodology, large steering angles are made accessible to an array by maximizing the width of the single element radiation pattern. A recent study details the influence of the substrate configuration on the radiation pattern of infrared dipole antennas [15]. To a first approximation, the angular response is determined by boundary conditions imposed on the radiated fields. For example, the radiation pattern in the H-plane of a dipole

on an interface is proportional to the squared norm of the transmission coefficient between the dielectrics [16]. If a ground plane is present, the transmission coefficient must be multiplied by an interference term to account for the image of the antenna generated by the conductive surface [15]. Of the various substrate configurations considered, a dielectric layer above a ground plane was found to exhibit the broadest radiation pattern, nearly twice as broad as the angular response of the same antenna fabricated on a hemispherical substrate. Therefore, one expects larger steering angles to be accessible with this configuration. In addition, the presence of a ground plane leads to enhanced field confinement within the substrate and thus to a resonance which is more sensitive to changes in antenna length [17].

In light of these developments, we revisit the possibility of controlling the angular response pattern of infrared phased array antennas. We do so by implementing a MOM diode to ensure that the measured response originates from a coherent summation of infrared antenna currents at a localized point in the array, and not from the distributed thermal response of the antenna, interconnects, and lead-lines. The reception angle of the antenna is altered by shifting the diode position along the CPS that connects the antenna elements. Substantial improvements in beam width and steering angle are realized by fabricating the antenna arrays on a fixed dielectric stand-off layer above a ground plane. Radiation patterns measured with a 10.6 μm CO_2 laser are corroborated with electromagnetic numerical simulations as well as an analytic interference model.

2. Model

Consider two dipole antennas connected by a CPS of length L, on a dielectric layer above a ground plane, with a diode placed a distance d from their common center, as shown in Fig. 1. One can derive an expression for the reception angle of the antenna from the array factor for a two dipole array. A plane wave polarized along the direction of the dipoles (shown in red) is incident on the antenna at an angle $θ$ measured from the surface normal in a plane perpendicular to the dipoles (H-plane).
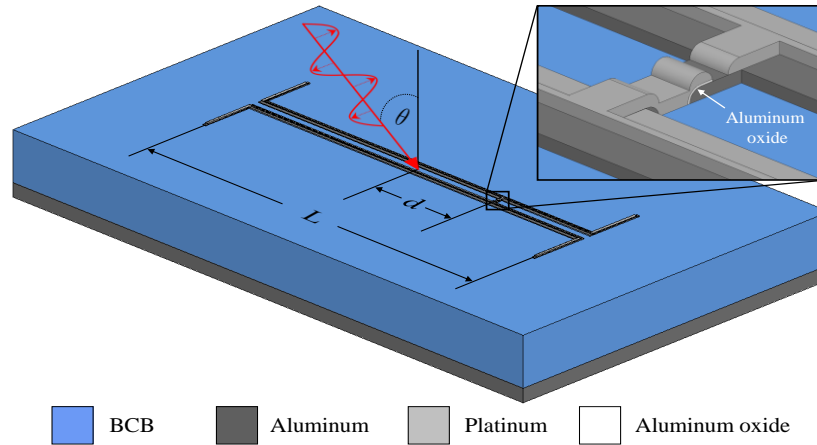

Fig. 1. Model of the antenna/substrate configuration and definition of terms. Superset image shows the aluminum-platinum overlap and the aluminum oxide barrier. The angle $θ$ is measured in the plane perpendicular to the dipoles (H-plane).

The radiation arriving at the detector will include a phase shift due to free space propagation that is angle dependent as well as an interelement phase shift acquired during propagation along the CPS. Constructive interference occurs at the diode when the total phase difference is an integer multiple of $2π$,

$$\frac{2\pi}{\lambda_0} L \sin\theta_m - \frac{2\pi}{\lambda_0} 2n_m d = 2\pi m, \qquad (1)$$

where λ_0 is the wavelength in free space and n_m is the effective index of the CPS mode. The response angle of the antenna array corresponds to the primary maximum in the interference pattern. Inserting m = 0 into Eq. (1),

$$\theta_0 = \sin^{-1}\left(\frac{2n_0 d}{L}\right). \tag{2}$$

As one might expect, the response angle of the antenna increases as the diode is shifted away from the center of the dipoles. For diode shifts that are small compared to the antenna spacing, the reception angle varies approximately linearly with the diode shift as $\theta_0 \cong 2n_0 d / L$. The magnitude of the response angle is determined by the ratio of the diode shift to the dipole separation.

The diode under investigation is an asymmetric structure comprised of aluminum, aluminum-oxide and platinum. The device operation, including *I-V* characteristics and fabrication parameters, is detailed in the literature [18,19]. Infrared radiation transferred from the dipole antennas along the CPS to the aluminum-oxide barrier can be expressed as a time varying optical voltage [20],

$$V(t) = V_b + V_0 \cos(2\pi f t), \tag{3}$$

where V_b is the bias voltage, V_0 is the amplitude of the induced voltage, and *f* is the frequency of the infrared radiation. When the optical voltage has the same polarity as the work function difference between aluminum and platinum, the separation between the Fermi levels increases and the thickness of the potential barrier will decrease. Consequently, the probability for electrons to tunnel through the oxide increases.

An analytical expression for the rectified current I_r can be obtained by evaluating the time average of the current when expanded in a power series with respect to voltage [21]. The first nonzero term in the time average is the rectified current

$$I_r = \frac{1}{4}\frac{d^2 I}{dV^2}\bigg|_{V=V_b} V_0^2. \tag{4}$$

Here the proportionality constant is the second derivative of the *I-V* characteristic evaluated at the bias voltage. Thus, the rectified current is proportional to the square of the amplitude of the optical voltage, and therefore, to the infrared power at the MOM junction.

Numerical simulations are performed in Ansoft High Frequency Structure Simulator (HFSS), a commercial electromagnetic finite element solver. The full antenna structure is modeled in HFSS, including the Al-Pt overlap from the shadow evaporation (discussed in section 3) and the intermediate aluminum-oxide barrier. Both are shown in Fig. 1. From Eq. (4), a quantity proportional to the rectified current is computed as the time averaged power density integrated over the surface area of the aluminum-oxide layer. For a thin oxide, the dominant contribution arises from surfaces with their normals parallel to the current flow. Therefore, integration yields the optical power flow through the oxide layer. Upon excitation of the antenna with a Gaussian beam of waist w_0 = 115 μm and wavelength 10.6 μm (28.3 THz), the electromagnetic fields are calculated everywhere within the solution volume. To generate a radiation pattern, the total power flow through the oxide is computed for each angle of incidence. The material properties, including refractive index and thickness, are measured using a J.A. Woollam Infrared Variable-Angle Spectroscopic Ellipsometer (IR-VASE) and subsequently incorporated into the numerical models to increase the accuracy of the simulations [22].

3. Method

Figure 2 contains scanning electron micrographs (SEM) of two completed antenna-coupled MOM diode devices. The topmost, symmetric antenna is designed for broadside or normally incident illumination. In this case, the diode is centered between the dipole antennas. The

bottommost antenna has the diode shifted $d = 3.3$ μm from center. This design is optimized for response at 50°. A high magnification SEM shows a MOM diode that is circular in shape and approximately 100 nm in diameter.
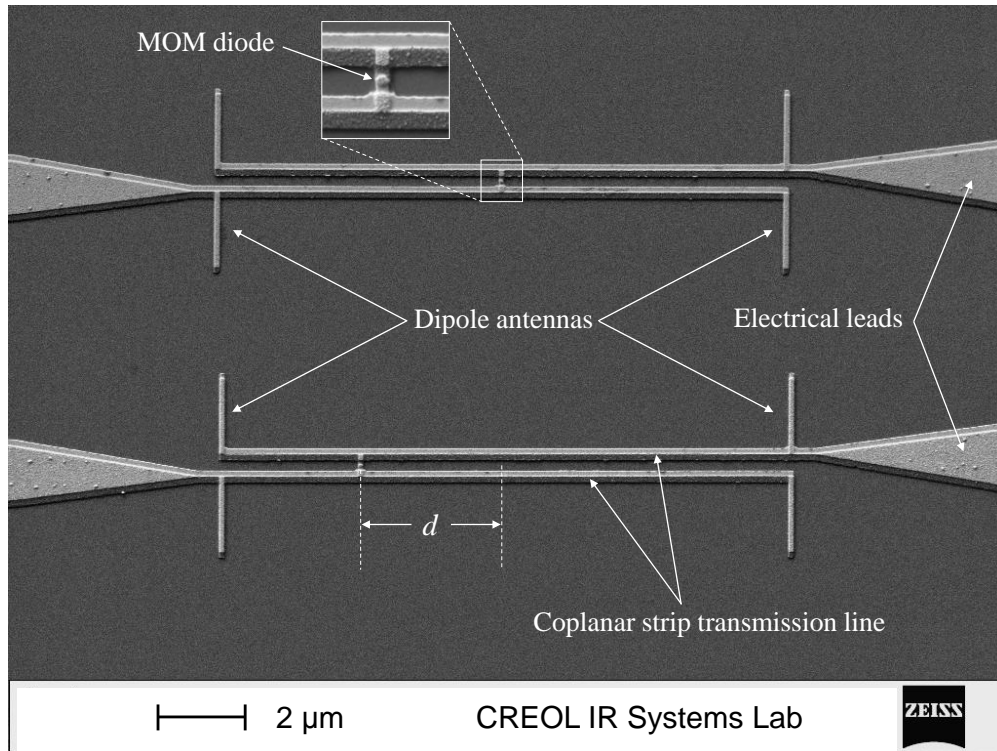

Fig. 2. Scanning electron micrograph of the phased-array antenna with (top) a centered diode and (bottom) with the diode shifted by $d = 3.3$ μm. Superset SEM of the MOM diode shows an overlap that is circular in shape and approximately 100 nm in diameter.

The coupling efficiency and attenuation constant of a CPS are determined by the strip separation and substrate material, respectively. To minimize absorption by the substrate, the CPS mode should lie symmetrically about the dielectric-air interface. To this end, we choose benzocyclobutene (BCB), a low loss insulator ($k = 0.015$) with a refractive index close to that of air ($n = 1.55$) in the 10.6 μm infrared region. To optimize the coupling efficiency from the antenna to the CPS, the diode response is monitored in HFSS while varying the strip separation. Including the overlap from the shadow evaporation (discussed below), a separation of 230 nm yields the greatest antenna response. Similarly, one could attempt to optimize the coupling efficiency from the CPS to the MOM diode by changing the overlap area. The problem here is that the diode area is bounded from below by fabrication limitations and above by the requirement that the capacitance enable rectification at IR frequencies [12].

The rectified current at the MOM junction is proportional to the optical power, or equivalently, the square of the electric field. For a half-wave dipole, the field will be a maximum at its center. Therefore, the rectified current will be maximized when the antennas are designed to resonate at one-half wavelength. For a BCB-air interface, the effective index is $n_{eff} \approx 1.3$, corresponding to an effective half-wavelength for the dipole of $\lambda_0 / 2n_{eff} \approx 4$ μm [23]. This value is also identified in numerical simulations as the dipole length that generates the greatest response.

A parametric analysis is performed in HFSS to maximize the width and uniformity of the single element pattern. As the BCB thickness increases from zero, the radiation pattern broadens until it reaches a maximum width when the BCB thickness is one quarter

wavelength. Beyond this, the radiation pattern develops a null at broadside. The optimal radiation pattern occurs for a thickness of 1.8 μm.

According to Eq. (2), the response angle of the antenna depends only on the ratio of the diode shift to the antenna spacing. However, one must also consider the near fields produced by the dipole antennas, and the effects they might have on the measured response [24]. To avoid any near field interference, the antenna spacing should be sufficiently large so that the diode is removed from the reactive near field of the dipole antennas, which is generally taken to be around one quarter of the effective wavelength [14], or about 2 μm on BCB. By setting $d = 0$ and m = 1 in Eq. (1), one finds that the width of the main lobe in the radiation pattern varies as λ_0 / L so that larger antenna spacings produce narrower beam widths. However, as the antenna spacing increases, the infrared currents must travel a greater distance to reach the diode, and will thus be subjected to more attenuation. Moreover, the side lobe contribution generally increases as the antenna spacing increases. Therefore, one chooses the maximum antenna spacing that simultaneously minimizes propagation loss and side lobe level. Numerical simulations that include the measured material properties infer an optimal antenna spacing of $L = 12.9$ μm.

Fabrication of infrared antenna-coupled MOM diodes is well documented [13,23]. The process includes electron beam lithography and a shadow evaporation consisting of two metal depositions and an intermediate oxidation step. Evaporation at two opposing angles generates a small area, typically 75×75 nm, where the two metals overlap beneath a bridge of undercut electron beam resist. The entire antenna structure, including the lead lines, CPS, and diode are metalized during a single shadow evaporation. To replicate an ideal point load, the electrical resistance of the MOM diode should be much greater than the combined resistance of the antenna, lead lines, and bond pads, which is typically around 300 Ω. Therefore, an oxidation pressure of 100 mtorr is used to produce approximately 2 nm thick diodes with dc resistances on the order of 100 kΩ [19].

4. Results

A CO_2 laser operating at 10.6 μm is chopped at 1.5 kHz and focused at F/8 onto the antenna, which is connected to a five axis goniometer [25]. The device is connected to a current preamplifier and monitored with a lock-in amplifier that is referenced to the frequency of the mechanical chopper. Temporal fluctuations in the laser power are removed by dividing the device response by the reference power. During an H-plane radiation pattern measurement, the polarization of the laser is oriented along the dipole antennas while the goniometer is rotated in the plane perpendicular to the axis of the dipoles, as illustrated in Fig. 1. Five averaged measurements are taken at each angle of incidence from −70° to 70°. All measurements are conducted without applied bias and with a beam irradiance of approximately 10 W cm^{-2}, well within the region where the MOM diode acts as square law detector [19]. To ensure that the measured response originates from the rectified current and not from bolometric sources, each device response is observed for radiation polarized perpendicular to the dipoles. For all devices, the magnitude of the cross polarized response is nearly equal to the Johnson noise, which can be taken as an indication that the thermal response is negligible.

The measured and simulated radiation patterns in the H-plane of a single dipole on a 1.8 μm BCB stand-off layer above a ground plane are shown in Fig. 3. Both the measurement and simulation are normalized to their maximum values. The radiation patterns are plotted linear in power to emphasize the square law behavior of the MOM diode. As expected, the single element radiation pattern is uniform and broad, with a FWHM of 140°. Since the overall radiation pattern is given by the product of the array factor and the single element pattern, Fig. 3 represents the range of reception angles that is accessible to an array. Excellent agreement is observed between the measured and simulated radiation patterns.
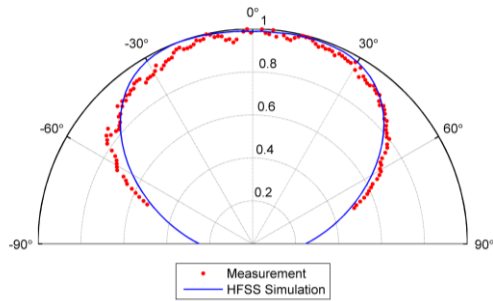
Fig. 3. Measured and simulated radiation pattern (linear in power) of a single dipole on a 1.8 μm BCB stand-off layer above a ground plane.

Figure 4 shows the measured radiation patterns along with the HFSS simulations for antenna arrays with diode shifts of $d = 0$, 0.9, 1.8, and 3.3 μm. Over this range, the response angle of the antenna varies from 0° to 50°. Negative angles can be easily obtained by shifting the diode in the opposite direction. As the response angle increases, the FWHM increases slightly from 30° to 40° while the side lobe magnitude increases from 5% to around 25%. Excellent agreement between simulation and measurement is observed for both the response angle and beam width.
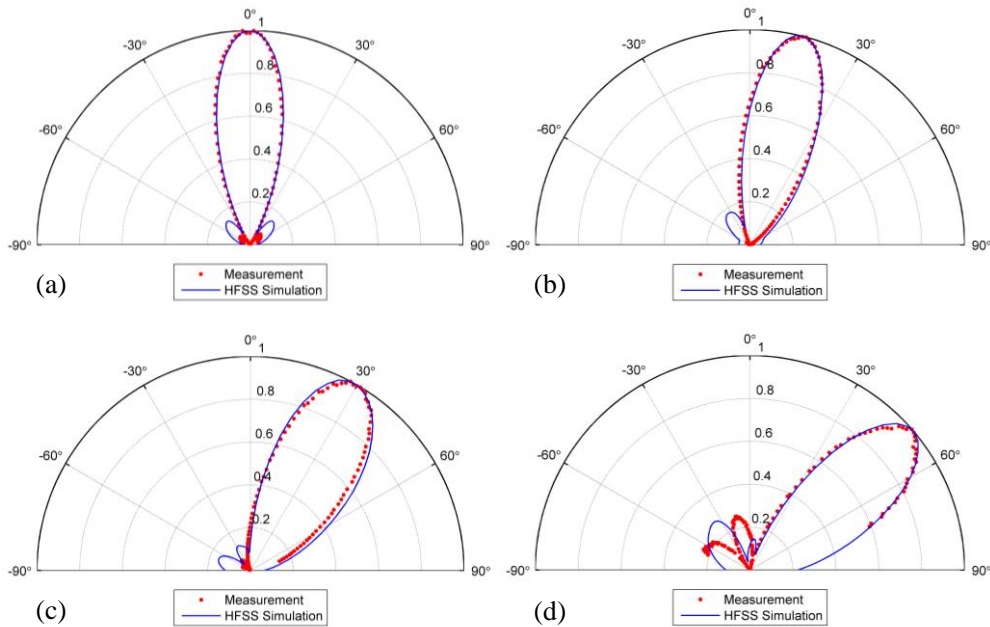

Fig. 4. Measured and simulated radiation patterns (linear in power) of a dipole pair antenna on a 1.8 μm BCB stand-off layer above a ground plane with the diode shifted (a) $d = 0$ μm, (b) $d = 0.9$ μm, (c) $d = 1.8$ μm and (d) $d = 3.3$ μm.

Moderate discrepancies between simulation and measurement are apparent in side-lobe magnitude and angle, which may be attributed to alignment errors and uncertainty in the local substrate thickness. The alignment procedure ensures that the device is simultaneously aligned with the axis of rotation of the goniometer and focus of the laser beam to within approximately ± 12 μm. For a Gaussian beam of waist $w_0 = 115$ μm, a device displaced 24 μm in a direction perpendicular to the beam path would experience an 8% reduction in power density, which partially accounts for the discrepancy in the side lobe level. In the simulations, the side lobe level is determined by the single element pattern, which depends primarily on

the thickness of the dielectric layer. From ellipsometric measurements performed on the actual substrate containing the devices, the percentage deviation from the measured thickness is ± 1.6%, significant enough to impact the side lobe level in the simulations. Since the exact substrate thickness in the vicinity of each device is unknown, the best one can do is set the thickness in HFSS to the value measured with the infrared ellipsometer, which is essentially an average over an approximately 8 mm diameter beam.

A plot of the measured and simulated response angle as a function of the ratio of the diode shift to the antenna spacing is shown in Fig. 5. The response angle is taken to be the angle where the radiation pattern is a maximum. When the diode shift is small compared to the antenna spacing, the response angle varies linearly with the diode position, as prescribed by Eq. (2). For diode shifts greater than approximately one quarter of the antenna spacing, the response angle levels off, reaching a maximum around 53°. Since the total radiation pattern is given by the product of the array factor and the single element pattern, the maximum response angle of the array corresponds to the angle where the single element pattern decreases rapidly. From Fig. 3, this occurs around 55°. Moreover, as the main lobe shifts towards large angles, the side lobes are magnified as they approach broadside. Consequently, response angles beyond 50° are accompanied by an equal or greater side lobe response.
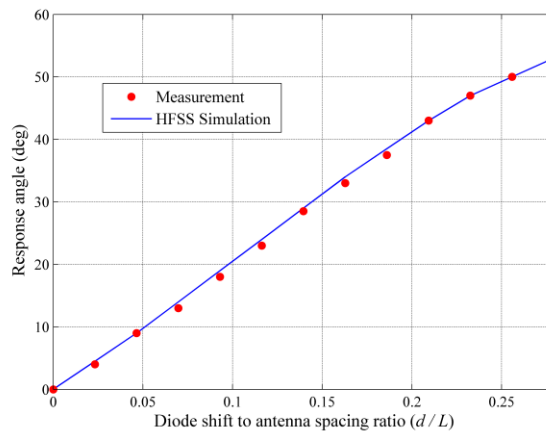

Fig. 5. Measured and simulated response angle as a function of the diode shift to antenna spacing ratio d / L. All devices are fabricated on a fixed 1.8 μm BCB stand-off layer above a ground plane.

5. Conclusion

Directional control of received infrared radiation is demonstrated with a phased array antenna coupled to a metal-oxide-metal tunnel diode. We implement a MOM diode to ensure that the measured response originates from a summation of infrared antenna currents at a localized point in the array. To achieve large response angles, the width of the single element radiation pattern must be broad. This can be realized with a substrate configuration consisting of a 1.8 μm BCB stand-off layer above a ground plane. With the substrate configuration fixed, reception angles of ± 50° are attainable by shifting the position of the diode along the CPS that connects the dipoles. This can be interpreted with an analytic interference model that accounts for the interelement phase difference that is introduced by the diode shift. The measured radiation patterns are in excellent agreement with electromagnetic simulations performed in Ansoft HFSS as well as the analytic interference model. Applications for a low-cost, uncooled, phased-array antenna in the thermal infrared band include coherence detection and rudimentary lensless imaging.